Geophysical Research Letters

Key Points:
- Ocean-bottom Distributed Acoustic Sensing is used to image shallow V_S structure
- Rayleigh wave phase velocity dispersion curves are extracted from frequency-wave number analysis
- Reflection image is obtained from autocorrelations of ambient seismic field

Supporting Information:
- Supporting Information S1

Correspondence to:
Z. J. Spica,
zspica@umich.edu

Marine Sediment Characterized by Ocean-Bottom Fiber-Optic Seismology

Zack J. Spica[1,2] , Kiwamu Nishida[3] , Takeshi Akuhara[3] , François Pétrélis[2,4] , Masanao Shinohara[3] , and Tomoaki Yamada[2,5]

[1]Department of Earth and Environmental Sciences, University of Michigan, Ann Arbor, MI, USA, [2]Formerly at Earthquake Research Institute, The University of Tokyo, Tokyo, Japan, [3]Earthquake Research Institute, The University of Tokyo, Tokyo, Japan, [4]Laboratoire de Physique de l'École Normale Supérieure, ENS, Université PSL, CNRS, Sorbonne Université, Université Paris-Diderot, Sorbonne Paris Cité, Paris, France, [5]Japan Meteorological Agency, Tokyo, Japan

Abstract The Sanriku ocean-bottom seismometer system uses an optical fiber cable to guarantee real-time observations at the seafloor. A dark fiber connected to a Distributed Acoustic Sensing (DAS) interrogator converted the cable in an array of 19,000 seismic sensors. We use these measurements to constrain the velocity structure under a section of the cable. Our analysis relies on 24 hr of ambient seismic field recordings. We obtain a high-resolution 2-D shear-wave velocity profile by inverting multimode dispersion curves extracted from frequency-wave number analysis. We also produce a reflection image from autocorrelations of ambient seismic field, highlighting strong impedance contrasts at the interface between the sedimentary layers and the basement. In addition, earthquake wavefield analysis and modeling help to further constrain the sediment properties under the cable. Our results show for the first time that ocean-bottom DAS can produce detailed images of the subsurface, opening new opportunities for cost-effective ocean-bottom imaging in the future.

Plain Language Summary Distributed Acoustic Sensing (DAS) is a relatively new measurement method that has the potential to convert existing fiber optic communication infrastructure into arrays of thousands of seismic sensors. In this research, we connected a DAS to a cable that was originally installed at the bottom of the ocean to sustain a seismic and tsunami observatory in the Sanriku Region. We show that this new type of measurement can provide reliable information to image and explore the shallow subsurface under this fiber cable. This is the first time such analysis is performed in an oceanic environment, and our methods could be readily exportable to other fiber-optic cables that are the backbones of our modern telecommunication.

1. Introduction

The accurate determination of models of the shear velocity of marine sediments has significant implication for many different fields both in academia and industry. For geotechnical applications, such as the construction of offshore platforms and pipelines, these models provide constraints on the shear modulus (Ayres & Theilen, 2001) and allow quantifying sediment stability and earthquake amplification effects (Akal & Berkson, 2013; Sanchez-Sesma, 1987). For seismic imaging, shear-wave velocity models are required to improve the processing algorithms for multicomponent seismic data like static correction for converted *PS* waves (e.g., Muyzert, 2000), wavefield separation (e.g., Schalkwijk et al., 2000), or other imaging techniques with phase conversion (e.g., Akuhara et al., 2019). Also, combination of both *S* and *P* wave velocities helps to better interpret the lithology because together they are much more sensitive to fluid and gas contents than *P* wave alone (Ayres & Theilen, 2001).

Other than direct core sampling, our knowledge of the shear-wave properties of the sediments is largely based on active and passive seismic surveys (e.g., Mordret et al., 2013; Socco et al., 2011). With active seismic, measurements of sediment shear-wave speed are problematic because active sources in water require strong energy conversion to produce significant body shear wave on seafloor. As a result, simple evaluation of the shear-wave structure lags far behind the detailed 3-D mapping techniques existing for *P* wave (e.g., Vardy et al., 2017). Therefore, both active and passive methods generally promote the use of the low-frequency solid-liquid interface waves (a.k.a. Scholte waves Nolet & Dorman, 1996; Scholte, 1958) to constrain the

shear-wave structure in water (e.g., Kugler et al., 2007; Ritzwoller & Levshin, 2002). These surface waves can be retrieved from active *P* wave seismic records but are also naturally and permanently generated by the ocean mass movements. Indeed, the interactions of surface gravity waves are at the origin of the secondary microseism (e.g., Ardhuin et al., 2011; Hasselmann, 1963; Longuet-Higgins, 1950), which is the main seismic source used in offshore ambient seismic field (ASF) correlation studies (e.g., Mordret et al., 2014; Yao et al., 2011). Although these methods may provide high resolution, they are usually limited in extent (e.g., Kugler et al., 2007; Mordret et al., 2013). The development of large-scale seismic experiments involving the deployment of multiple ocean bottom seismographs (e.g., Kanazawa et al., 2016) has offered the opportunity to constrain sediment thickness over larger areas but at the cost of a much lower resolution. In addition, certain of these seismic networks are restricted in time (from a few months to approximately a year), limiting their potential for continuous monitoring (e.g., Shinohara et al., 2012). An appealing alternative is the emerging technology of Distributed Acoustic Sensing (DAS) that turns fiber-optic cables into thousands of seismic sensors (Grattan & Sun, 2000; Posey Jr. et al., 2000). The fiber is probed by repeated laser pulses, and an interferometer analyzes the backscattered light to measure the deformation (strain) along the fiber due to its interaction with seismic waves. The obtained waveforms at each channel are then not point measurements but rather are strains measured over a spatial distance (the gauge length) in the direction of the cable. As the fiber is a passive component, no extra electronic device is needed, and the fiber may be left on the ocean floor for a virtually unlimited amount of time. The fiber offers real-time telemetry for thousands of synchronized sensors and works on one single power source. Furthermore, fiber cables abound in certain oceanic regions as they are the backbone of telecommunication networks. Lately, ocean-bottom DAS prototype experiments have shown promises to monitor the ocean-solid earth interactions and to detect oceanic seismicity with signal characteristics comparable to those of ocean-bottom seismometers (OBS) (Lindsey et al., 2019; Shinohara et al., 2019; Sladen et al., 2019; Williams et al., 2019).

In this communication, we demonstrate for the first time that DAS can be used to passively image shallow sediments at the bottom of the ocean. Our analysis relies only on 1 day of ASF recorded with a fiber cable originally installed for telecommunication between OBS systems in the Sanriku Region, Japan (Figure 1). ASF is used to extract multimode Rayleigh wave dispersion curves that we invert locally to provide a 2-D shear-wave velocity profile under a section of the cable with a resolution and an extent that would be hard to obtain with traditional OBS or hydrophone arrays. In addition, autocorrelations of ASF computed for the first ~10,000 channels of the array deliver a reflection image of the shallow sedimentary layers. This image sheds light on strong impedance contrast and possible sharp amplification of seismic waves in a particular region of the continental slope in connection with extremely low-velocity sediments. Our approaches do not require costly offshore dedicated survey, can be repeated at different times at almost no additional cost, and could be readily exported to other existing ocean-bottom fiber cables worldwide to provide high-resolution structural images of the ocean-bottom seismic properties.

2. Materials and Methods

2.1. The Sanriku Fiber Cable

DAS is particularly cost-effective if a preinstalled fiber-optic cable is available. Here, we take advantage of one submarine telecommunication cable system (Figure 1) that was installed in 1996 to sustain an ocean-bottom seismic observatory (Kanazawa & Hasegawa, 1997) located near the source area of the 2011 Tohoku-Oki Earthquake (e.g., Suzuki et al., 2011). The system is composed of a 120-km cable with three three-component accelerometers and two pressure gauges. Although the great Tohoku-Oki Earthquake damaged the landing station, the cable system was restored in 2014 (Shinohara et al., 2016). According to the installation report, the cable is buried 0.6–0.7 m below the seafloor from the coast until the point where the water column reaches 997 m (i.e., ~47.7 km from the landing station). A DAS interrogator unit with a 100-km sensing range (AP Sensing N5200A, Cedilnik et al., 2019) was connected to the landing end of the fiber, and data were acquired at 500 Hz for about 46 hr starting on 13 February 2019. The gauge length was initially set to 10 m, but it was changed to 40 m after about 90 min of recordings. The spacial sampling was set to 5 m, yielding to an array of ~19,000 horizontal channels along the first 100 km of the cable. In this contribution, we use the 40-m gauge length and only analyze the first ~48 km, which corresponds to the buried section of the cable where we can guarantee a better coupling between the cable and the seafloor. Both the DAS and the OBS system were operational during the experiment. More details about the cable setup and measurement quality can be found in Shinohara et al. (2019).
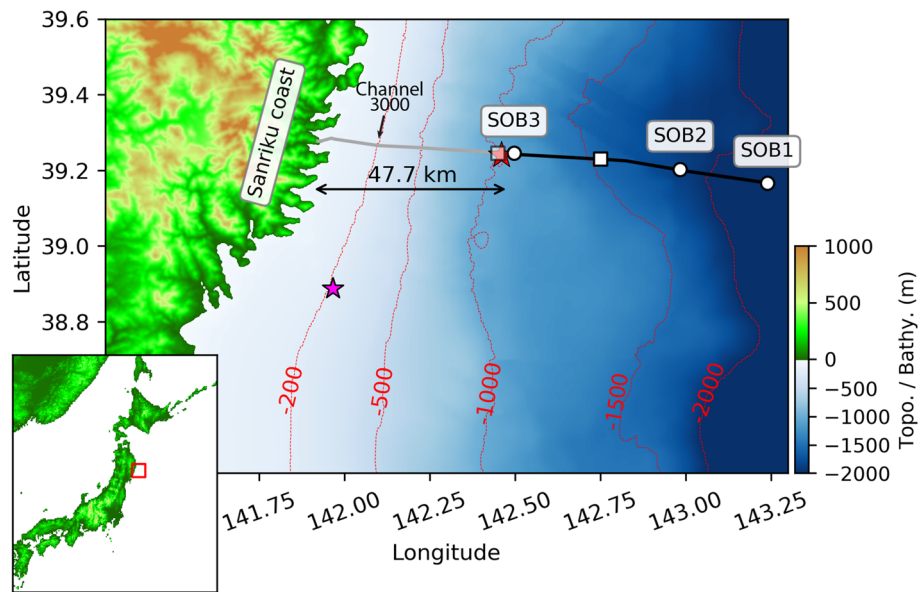
Figure 1. Map showing the location of the telecommunication fiber-optic cable off the shore of Sanriku. The gray section of the cable, which is used in our analyses, is buried under 60–70 cm of sediment, while the black section lies directly on the seafloor by gravity. The white dots depict the accelerometers, and the white squares are the pressure gauges. The pink star depicts the location of an earthquake (2019-02-14T21:10:50; $M_w = 3.0$) recorded by DAS and shown in Figure 3c. The red star depicts the location of another earthquake recorded only by the OBS systems (2018-01-30T17:20:56.31; $M_w = 3.1$; depth = 30.9 km) and showed in Figure 4.

2.2. 2D Shear-Wave Velocity Profile

2.2.1. Phase Velocity From Frequency-Wave Number Analysis

Applying a 2-D Fourier transform to a 2-hr strain record of a group of channels allows identification and separation of coherent oceanic and seismic signals in the frequency-wave number (FK) domain. Figures 2 and S1 in the supporting information show the FK power spectrum for a subset of 1,000 channels centered on Channels 3,000 and 8,000, respectively. Given the linear geometry of the cable, the observed signals can be easily interpreted for both incoming (landward) and reflected energies. Such spectral analysis can also be repeated along the length of the buried cable with a moving window of 500 channels to evaluate the fluctuations of the wave energies as a function of distance from the coast or depth (Figure 3a).

Ocean surface gravity waves appear at frequencies lower than ~0.2 Hz near the coast and with peak frequency under 0.12 Hz off the coast (Figures 2 and 3a). In Figure 2c ″, they show an apparent phase velocity of ~40 m/s, when projected in the frequency-phase velocity space. Their attenuation with depth and their dispersion follow the linear gravity wave theory ($\omega^2 = gk \tanh(kH)$; e.g., Gill, 1982), meaning that these coherent seismic energies represent the generation of primary microseisms in situ (e.g., Williams et al., 2019). Although of interest, the detailed analysis of these surface gravity waves propagating across the array is out of the scope of this contribution.

When surface gravity waves interfere nonlinearly with nearly opposite wave numbers, they generate a double-frequency pressure fluctuation that can propagate efficiently in the deep waters until and through the seabed (e.g., Ardhuin et al., 2011; Hasselmann, 1963; Longuet-Higgins, 1950). This phenomenon is at the origin of the secondary microseisms and is well observed in our data at depths greater than ~150 m (Figure 3a). Figures 2c and S1c show distinct dispersive wave packets with dominant frequencies at ~0.75 and ~0.5 Hz, respectively. Both show phase velocities ranging from ~300–600 to ~1,500 m/s, suggesting that they are seismo-acoustic surface waves controlled by the properties of the shallow sediments and the speed of acoustic waves in water (Williams et al., 2019). These dispersive waves are most likely Scholte waves, as the fiber-optic DAS is more sensitive to longitudinally propagating waves than horizontally polarized waves with motion almost perpendicular to the cable (i.e., Love waves).

Numerical calculation of dispersion curves (Herrmann, 2013) for a known velocity model of the region (Figure S2) further suggests this hypothesis as it approximates fairly well the fundamental and higher modes
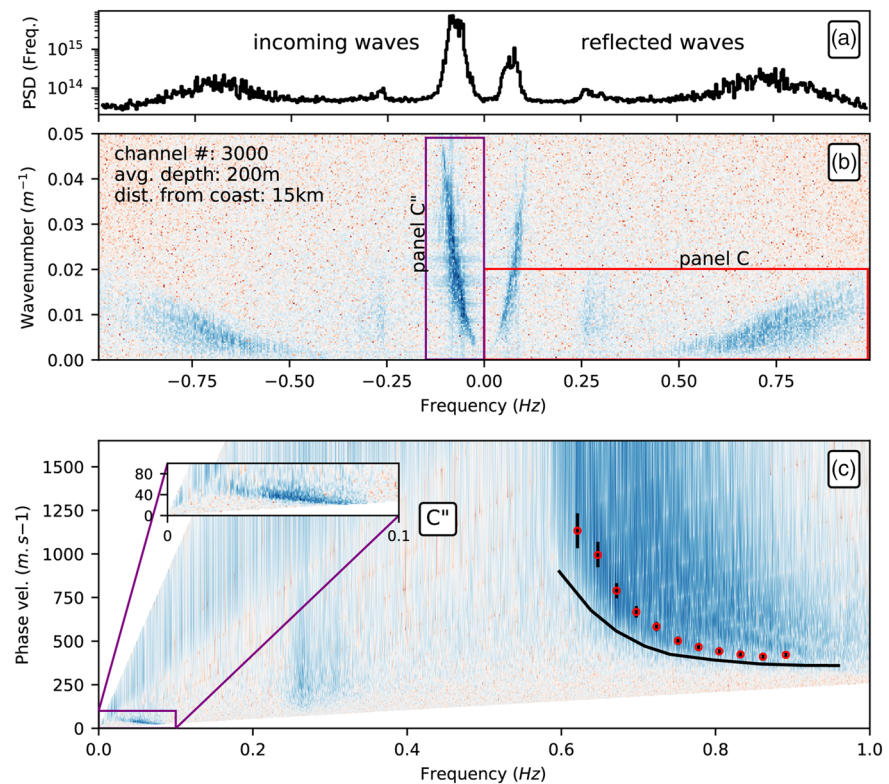
Figure 2. (a) Power Spectral Density of panel (b). (b) FK power spectrum of a subset of 1,000 channels centered on Channel 3,000. The colored boxes highlight the region used to compute panels (c) and (c″). (c) Same as the red region in (b) but after conversion to the phase velocity frequency domain. Black line depicts the fundamental mode of the Scholte waves for a suggested velocity model shown in Figure S2. Red dots with error bars are the extracted phase velocity used for inversion. (c″) Same as the purple region in (b) but after conversion to the phase velocity frequency domain and where we observe the dispersion of the ocean gravity waves.

observed in Figure S1c (black lines). In the region, the P wave velocity (V_P) of the Neogene marine sediment is ~2,400 m/s (Kodaira et al., 2017), and S wave velocity (V_S) can be approximated to ~600 m/s using a V_P/V_S of ~4 (Nakamura et al., 2014). The thickness has been reported as 1,200–1,800 m (Kodaira et al., 2017). The V_P and V_S of the Cretaceous basement near its top are ~4.7–5.5 and ~2.4–2.7 km/s, respectively (Kodaira et al., 2017; Shinohara et al., 2008). The densities of the sediments and the basement in the northwest Pacific are reported as ~1.350 and 2.750 g/cm^3, respectively (Kanazawa et al., 2001). On the other hand, to approximate the higher-frequency dispersive signal at Channel 3,000 (Figure 2c, black line), a much lower velocity ($V_S = 300$), a thinner sediment layer, and a V_P/V_S ratio of 8 (e.g., Nakamura et al., 2014) are needed. The velocity models used in this analysis are shown in Figure S2.

We extracted these phase velocity dispersion curves by selecting the local maxima in a given region of the FK power spectrum. This process was performed using a graphical user interface that involves visual validation of the dispersion curves (e.g., Spica et al., 2015). Validation is guided through theoretical dispersion curves for estimated velocity models of the region, as describe above. This process was performed for 45 locations along the cable (each ~1,000 m). When present in the data, both fundamental and higher modes were extracted. The error on the picking is intrinsic to the size of the bin in which the maximum is selected. This leads to a much larger error at higher velocities (Figure 2c).

2.2.2. Inversion for Shallow Shear-Wave Estimates

The dispersion curves were resampled using a polynomial function and then inverted using a simulated annealing algorithm that minimizes the misfit value calculated as the semblance between the data and the synthetics. Then, the inversion algorithm switched to nonlinear optimization procedure (gradient method) to reach the global minimum faster (e.g., Perton et al., 2017). The inversion was performed for thickness and S wave velocity for two layers overlying a half-space. The first initial velocity model was constrained based on our previous estimation of the velocity model (section 2.2.1), and then the initial velocity model
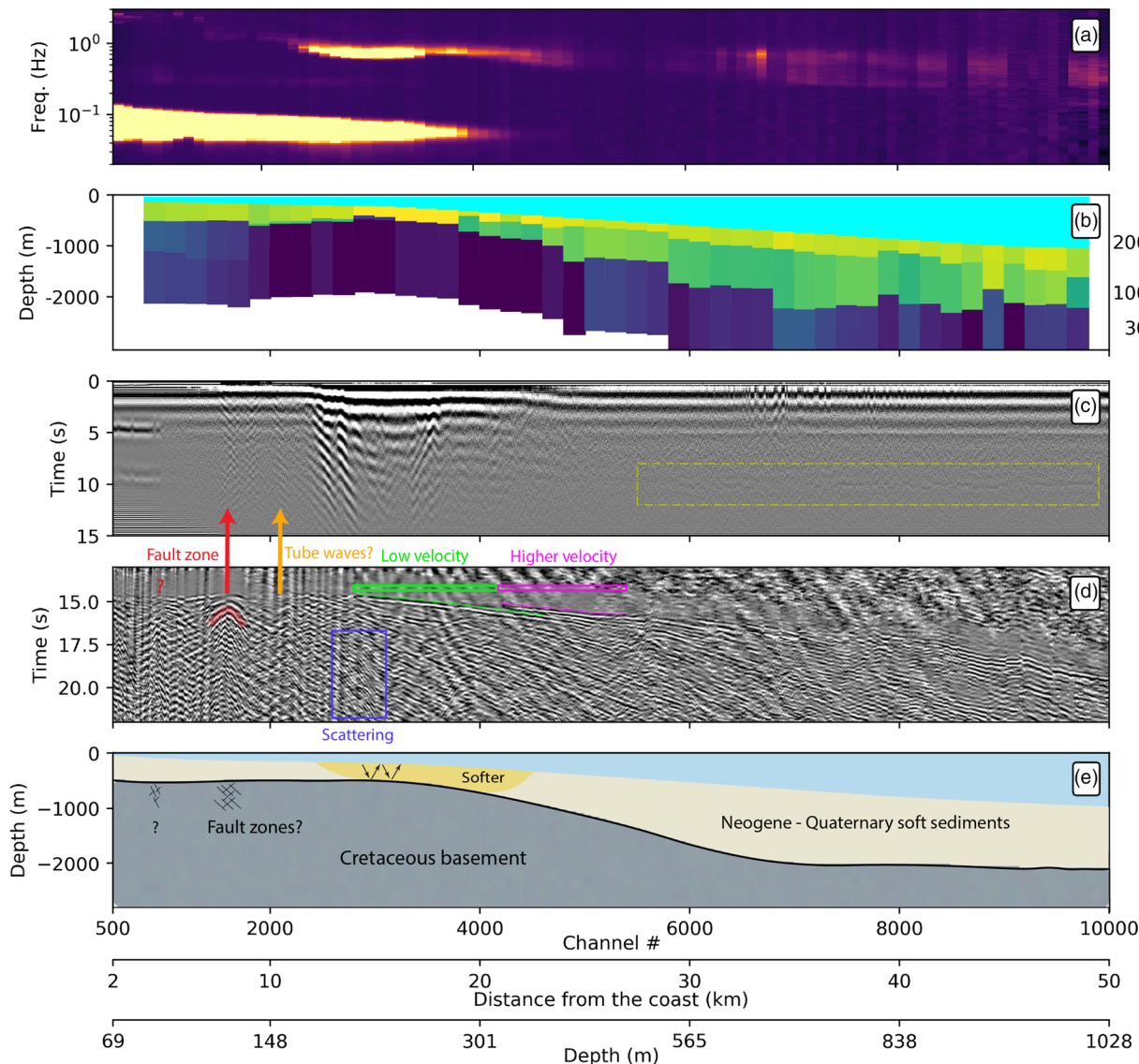
Figure 3. (a) Power spectral densities along the cable every 500 channel, as shown in Figure 2a (oceanward). (b) Two-dimensional shear-wave velocity profile obtained from the inversion of the dispersion curves at each subset of 1,000 channels, as shown in Figure S3. (c) Reflection image from autocorrelations of ASF. All autocorrelation functions are band-pass filtered between 0.8 and 4.5 Hz. The yellow box highlights potential velocity contrast corresponding to a four-way travel time reflected S waves. A zoom in the yellow box is shown in Figure S4d. (d) S wave arrivals with automatic gain control for an earthquake recorded by the array as shown in Figure 1. In the green area, the S wave arrives after the S wave in the purple area, which suggests a lower velocity zone. The inverted V shapes that may characterize fault zones are highlighted with a red arrow and a red question mark. These fault-zone regions are sometimes associated with amplification effects observed in the autocorrelation functions. Other amplification or scattering effects (orange arrow and blue box) may also be explained by localized tube waves or basin-edge scattering. (e) Geological interpretation that combines the observations of all panels.

in the inversion was taken as the last output model of the previously inverted velocity model, providing a natural smoothing for the entire 2-D model. Examples of 1-D S wave velocity models for selected channels are shown in Figure S3, and the complete 2-D velocity profile is shown in Figure 3b.

Overall, the agreement between synthetics and observations is very good; however, we observe a light deterioration of this agreement at higher frequency near Channel 3,000. In this area of the cable, inverted velocities of the topmost layers appear to be as low as ~300 m/s, suggesting an extreme impedance contrast with the basement layers that displays an average shear-wave velocity of ~2,100 m/s. Elsewhere, we observe an average velocity of ~500–700 m/s for the shallow layers. From the west to the east of the cable, the sedimentary layer tends to get thicker.

2.3. Reflection Image From Autocorrelations

Based on an extensive theoretical and experimental work, the 1-D Green's function stems from averaging autocorrelation of recorded motions (e.g., Claerbout, 1968). Several studies have shown that these zero-offset correlations can be used to constrain the local structure beneath a seismic station (e.g., Buffoni et al., 2019; Clayton, 2020; Kennett et al., 2015; Oren & Nowack, 2016; Pham & Tkalčić, 2017; Romero & Schimmel, 2018; Ruigrok & Wapenaar, 2012; Saygin et al., 2017; Spica et al., 2017; Sun & Kennett, 2016; Taylor et al., 2016; Tonegawa et al., 2013); however, because the ASF is generally dominated by surface waves, sub-critical body wave reflections are somehow more challenging to extract. In addition, the convolution of a delta pulse at zero time lag with the effective noise source time function generates wide zero-lag side lobes that sometimes hide the shallow subsurface reflections (Romero & Schimmel, 2018). Therefore, adapted processing, such as frequency filtering and source deconvolution, must be carefully applied, and this processing may vary from one data set to another.

After downsampling the records to 25 Hz and removing major earthquakes, the autocorrelations were computed for each channel using 24 hr of ASF signal and with a moving window of 30 s with 50% overlap. We applied the phase-weighted stacking method to stack each window (Schimmel & Paulssen, 1997). Then, each individual autocorrelation is deconvolved by a source term computed as the moving average autocorrelation over 500 channels, centered on the selected channel. The removal of the source function allows revealing better variations in the lateral structure. The different steps of this procedure are illustrated in Figure S4, and the final image filtered between 0.8 and 4.5 Hz is shown in Figure 3c.

Figure 3c displays distinctive features between the western and eastern section of the cable. From channels ∼2,500 to ∼5,000, a coherent but complex reflection pattern is drawn by the autocorrelation functions. After channel ∼5,500, we observe a double reflection with opposite polarity at ∼4.9 and ∼9.8 s (yellow features in Figure 3c). The amplitude of the first reflection is much higher than the second one, and both of them are intermittently weakened in certain regions. Between channels 500 and ∼1,000, we observe another double reflection with much higher amplitude. As a whole, the reflection profile shows strong lateral variation, suggesting the presence of different volumetric heterogeneities under the cable.

3. Discussion

The wave propagation characteristics retrieved from ASF autocorrelations are not only closely related to the proportion of the different waves existing in the records but also on the frequency band and the component used as well as the geological structure under the cable. Here, we used a frequency band of 0.8–4.5 Hz, which is not expected to be contaminated by anthropological noise at the bottom of the ocean. Under 1 Hz, the signal is largely dominated by surface-wave energy (Figures 2 and 3a), while at higher frequency, we may expect more body wave contribution (e.g., Saygin et al., 2017). DAS channels are parallel to the cable axis (i.e., mostly horizontal), and as the DAS is primarily sensitive to waves traveling longitudinally along the cable (Martin et al., 2018), the extracted autocorrelation signals are most likely surface waves or body waves with motion parallel to the cable (Rayleigh or S waves) (e.g., Miyazawa et al., 2008; Spica et al., 2017; Tonegawa et al., 2013).

The most striking feature of the reflection image is observed from channel ∼1,200 to ∼5,000. Here, a strong coherent wavefield is drawn by the autocorrelation functions, and no sharp travel time is identifiable. This coherent wavefield appears where we observe the highest Scholte wave energy along the cable (Figure 3a). In this area of the cable, the inverted velocity profile indicates extreme low shear-wave velocities (∼300 m/s) for a thin sedimentary layer. Therefore, we hypothesize that the strong impedance contrast existing between the bedrock and the sedimentary layer promotes multiple reverberation and trapping of the surface waves in a low-velocity microbasin resulting in the reverberating pattern observed in this section of the cable (Figure 3e). Since sedimentary basin trapped waves arise from constructive interference of multiple reflections at the boundaries between the low-velocity sediments and high-velocity surrounding rocks, the features of trapped waves (including amplitudes and frequency contents) are strongly dependent on the basin geometry and physical properties. By combining the methods described here, we could therefore further resolve the geometry and seismic properties of a small low-velocity basin from tens to several hundreds of meters using the DAS records.

Figure 3d depicts the wavefield after the *S* wave arrival for a local M_w = 3 earthquake (Figure 1). Here, the *S* wave front arrives later in the green region (low velocity) than in the purple region (higher velocity), which further suggests the presence of a small low-velocity basin. To exemplify this connection, we computed a set of 2-D finite-difference seismograms (Li et al., 2014) with similar source parameter than the earthquake in Figure 3c (see Table S1). They are calculated with a two-domain (i.e., fluid and solid) velocity model that includes realistic bathymetry with different levels of smoothness along the fiber-optic cable (Koketsu et al., 2012) and to which we added a shallow, thin low-velocity layer (Figure S5a). The synthetic waveforms (Figure S5b) show not only a systematic delay in the low-velocity region but also the occurrence of strong basin-edge scattering.

Under the red arrow in Figure 3d, we observe coherent seismic energy propagating outward and showing apparent velocity of 400–600 m/s. This inverted V-shaped feature is characteristic of waveguide effects where seismic energy interacts with highly fractured medium or low-velocity fault zones (e.g., Lindsey et al., 2019). Interestingly, this effect is also visible in the reflection image (top of the red array in Figure 3c) suggesting strong reverberation of the ASF in a subvertical fault. However, similar features in the autocorrelations are not always associated with clear fault zones attributes in the earthquake records. For example, under the orange arrow in Figure 3d, the V shape is questionable. Other effects such as tube waves that occur when the cable is locally subvertical due to strong topographic changes may also provoke similar features in the recordings (Daley et al., 2013; Munn et al., 2017). Similarly, basin-edge effects, as observed in the synthetics (Figure S5b), can also create scattering in the earthquake wavefield and can further complicate such interpretation (blue box in Figure 3d).

In the eastern region of the cable, the *S* wave velocity of the shallow sediments is relatively low (∼600 m/s; Figure 3b), meaning that the wavelengths are lower than 400 m. This is significantly less than the sediment thickness (1,100–1,400 m), suggesting that a *S* wave reverberation could easily occur. In this case, the two phases of opposite polarity observed at ∼4.9 and ∼9.8 s can be seen as a two-way and a four-way travel time reflected *S* waves. In Figure 3c, the ∼4.9-s reflection might be still contaminated by the lower-frequency surface-wave side lobes; however, the second reflection at ∼9.8 s is well isolated from any other signal and marks a clear structural interface at depth (yellow box in Figure 3c), although it has a much lower amplitude. Similar features were also observed to be persistent at OBS stations few hundreds of kilometers away from the Sanriku cable (Tonegawa et al., 2013).

In order to gain confidence in this interpretation, we analyzed an earthquake (M_w = 3.1) recorded by station SOB3 with a local incidence angle of ∼7° (Figure 1). We examined the waveforms after applying the rotation of the three components following Nakamura and Hayashimoto (2018) and a low-pass filter at 10 Hz (Figure 4). On the horizontal component parallel to the cable, a clear *P* to *S* converted wave appears ∼2.2 s after the *P* wave. As converted *S* waves typically happen at the bottom of sedimentary layers, their travel times may be used to quantify the thickness-velocity ratio of such sediment. In this case, a velocity of 600 m/s for a thickness of 1,200 m explains the observation, which therefore supports our previous interpretation and the inverted velocity model. Unfortunately, no clear *P* to *S* conversions were observed with DAS, probably because of its poor sensitivity to subperpendicularly incident *P* waves.

The inverted shear-wave velocity model and the reflection image suggest that the interface between sedimentary layers and Cretaceous basement is mostly horizontal in the eastern section of the cable from channel ∼6,000–10,000. Considering a vertical reflection at this interface, the horizontal geometry and the strong impedance contrast are favorable toward the retrieval of a sharp signal with displacement data (e.g., Tonegawa et al., 2013). On the other hand, because the strain is the derivative of the displacement ($\epsilon_{xx} = \frac{\partial u_x}{\partial x}$), a reflection between two perfectly parallel horizontal interfaces measured with DAS should be seen as null ($\frac{\partial u_x}{\partial x} = 0$). This may explain the low amplitude of the DAS *S* wave reflection signal; however, the fact that we observe it implicitly suggests a high level of roughness between the basement and the sedimentary layer. Such roughness at the interface between the sedimentary layers and the Cretaceous bedrock is very well reported by active source reflection profiling data taken at the vicinity of the cable (Geological Survey of Japan, 2013; Kodaira et al., 2017; Minoura et al., 2015). Finally, we acknowledge that another possibility to explain the detection of these somewhat surprising phases could be attributed to incomplete reconstruction
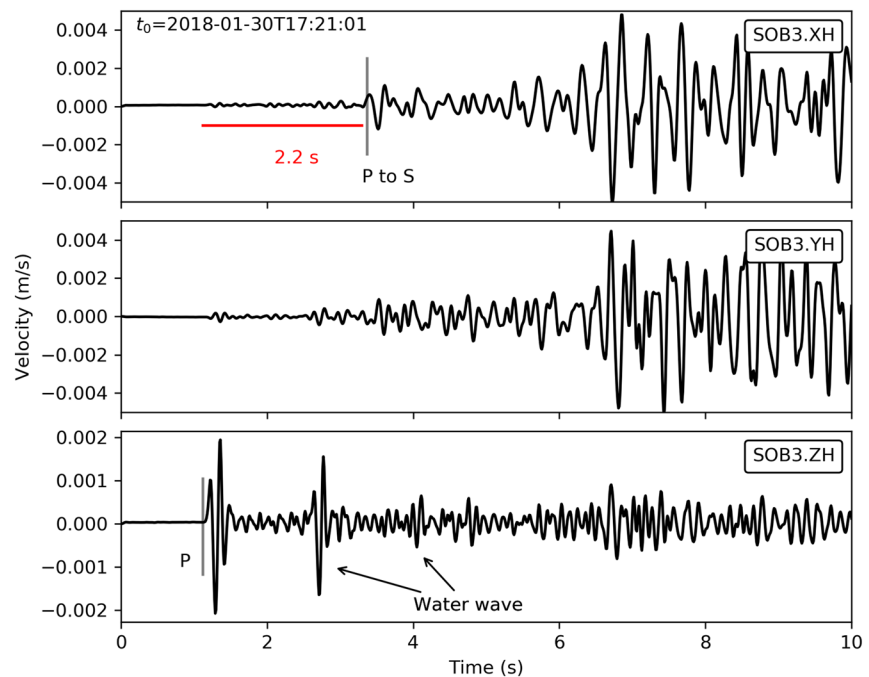
Figure 4. Earthquake recorded by OBS system SOB3, which highlights *P* to *S* conversion at the bottom of the sedimentary layer.

of the Green's functions by uneven noise sources distribution. The later may lead to the retrieval of strong amplitude spurious phases on the vertical components (e.g., Boué et al., 2013).

Our final interpretation of the marine shallow geology under the cable is described in Figure 3e.

4. Conclusions

We demonstrated for the first time that existing fiber-optic cable, otherwise employed for telecommunication between OBS, can also be used to image the properties of the shallow sediments at the bottom of the ocean and so at a resolution and a spatial extend hardly attainable with traditional active or passive seismic arrays. The only requirement is to connect a DAS interrogator to one end of the cable and record continuous seismic wavefield. As the fiber is a passive component, no other electronic equipment needs to be installed, and the fiber can be used for a virtually unlimited amount of time, providing a low-cost instrumentation of the ocean bottom.

As indicated in earlier prototype studies, we confirmed that ocean-bottom DAS is able to record both seismic waves and oceanic waves, meaning that a broad range of scientific applications can be explored with such technology. Here, we only used one day of continuous ASF to explore two potential applications of DAS for shallow imaging at the ocean bottom. First, we extracted multimode Scholte-wave dispersion curves from frequency-wave number analysis. These dispersion curves were then inverted to provide a 2-D profile of the shear-wave velocity. Second, we showed that dynamic strain DAS can provide 2-D reflection image using the autocorrelation method. The reflection image highlighted a potential two- and four-way travel time *S* wave reverberating at the bottom of a sedimentary layer and strong reverberations inside a low-velocity microbasin. These results are not only supported by the observation of extremely low sediment velocities and high amplitude of Scholte wave in the region but also by detailed inspection of earthquake wavefield and corresponding modeling. Furthermore, earthquake wavefield analysis allows us to highlight scattering effects associated with fault zones and sedimentary microbasin edges. Combining these techniques, the final interpretation of the marine shallow geology under the cable is sketched in Figure 3e.

The techniques presented here allowed us to further quantify the properties and geometries of the shallow Neogene marine sediments on top of a Cretaceous basement along 50 km of the fiber cable. Our results open new opportunities for ocean-bottom seismic imaging and exploration that could be performed in the future in a much more cost-effective way.

Data Availability Statement

The data useful to reproduce all the figures are available online (at https://doi.org/10.5281/zenodo.3928199). Waveforms for Figure 4 are available for download on the NIED website (https://www.bosai.go.jp/e/).

References

Akal, T., & Berkson, J. M. (2013). *Ocean seismo-acoustics: Low-frequency underwater acoustics*, vol. 16. United States: Springer Science & Business Media.

Akuhara, T., Bostock, M. G., Plourde, A. P., & Shinohara, M. (2019). Beyond receiver functions: Green's function estimation by transdimensional inversion and its application to OBS data. *Journal of Geophysical Research: Solid Earth*, *124*, 1944–1961. https://doi.org/10.1029/2018JB016499

Ardhuin, F., Stutzmann, E., Schimmel, M., & Mangeney, A. (2011). Ocean wave sources of seismic noise. *Journal of Geophysical Research*, *116*, C09004. https://doi.org/10.1029/2011JC006952

Ayres, A., & Theilen, F. (2001). Relationship between *P*- and *S*-wave velocities and geological properties of near-surface sediments of the continental slope of the Barents Sea. *Geophysical Prospecting*, *47*(4), 431–441.

Beyreuther, M., Barsch, R., Krischer, L., Megies, T., Behr, Y., & Wassermann, J. (2010). ObsPy: A Python toolbox for seismology. *Seismological Research Letters*, *81*(3), 530–533.

Boué, P., Poli, P., Campillo, M., Pedersen, H., Briand, X., & Roux, P. (2013). Teleseismic correlations of ambient seismic noise for deep global imaging of the Earth. *Geophysical Journal International*, *194*, 844–848.

Buffoni, C., Schimmel, M., Sabbione, N. C., Rosa, M. L., & Connon, G. (2019). Crustal structure beneath Tierra del Fuego, Argentina, inferred from seismic *P*-wave receiver functions and ambient noise autocorrelations. *Tectonophysics*, *751*, 41–53.

Cedilnik, G., Lees, G., Schmidt, P., Herstrøm, S., & Geisler, T. (2019). Ultra-long reach fiber distributed acoustic sensing for power cable monitoring. In *10th International Conference on Insulated Power Cables*. https://www.apsensing.com/fileadmin/Publication%20Files/Cedilnik_et_al._-_2019-Jicable-Proceedings-E4-4-Ultralong-reach-DAS-.pdf

Claerbout, J. F. (1968). Synthesis of a layered medium from its acoustic transmission response. *Geophysics*, *33*(2), 264–269.

Clayton, R. W. (2020). Imaging the subsurface with ambient noise autocorrelations. *Seismological Research Letters*, *91*(2A), 930–935.

Daley, T. M., Freifeld, B. M., Ajo-Franklin, J., Dou, S., Pevzner, R., Shulakova, V., et al. (2013). Field testing of fiber-optic distributed acoustic sensing (DAS) for subsurface seismic monitoring. *The Leading Edge*, *32*(6), 699–706.

Geological Survey of Japan (2013). 3.5khz SBP database.

Gill, A. (1982). Ocean-atmosphere dynamics. International Geophysics Series 30.

Grattan, K., & Sun, T. (2000). Fiber optic sensor technology: An overview. *Sensors and Actuators A: Physical*, *82*(1-3), 40–61.

Hasselmann, K. (1963). A statistical analysis of the generation of microseisms. *Reviews of Geophysics*, *1*(2), 177–210.

Heimann, S., Kriegerowski, M., Isken, M., Cesca, S., Daout, S., Grigoli, F., et al. (2017). Pyrocko - An open-source seismology toolbox and library. V. 0.3. GFZ Data Services. https://doi.org/10.5880/GFZ.2.1.2017.001

Herrmann, R. B. (2013). Computer proramms in seismology: An evolving tool for instruction and research. *Seismological Research Letters*, *84*, 1081–1088

Hunter, J. D. (2007). Matplotlib: A 2D graphics environment. *Computing in Science and Engineering*, *9*(3), 90–95.

Kanazawa, T., & Hasegawa, A. (1997). Ocean-bottom observatory for earthquakes and tsunami off Sanriku, north-east Japan using submarine cable, Paper presented at International Workshop on Scientific use of Submarine Cables, Comm. for Sci. Use of Submarine Cables, Okinawa, Japan (pp. 208–209).

Kanazawa, T., Sager, W., & Escutia, C. (2001). Proc. Odp, Init. Repts., 191, College Station, TX (Ocean Drilling Program).

Kanazawa, T., Uehira, K., Mochizuki, M., Shinbo, T., Fujimoto, H., Noguchi, S., et al. (2016). S-net project, cabled observation network for earthquakes and tsunamis. Abstract WE2B-3, Presented at SubOptic 2016 , 18-21.

Kennett, B., Saygin, E., & Salmon, M. (2015). Stacking autocorrelograms to map Moho depth with high spatial resolution in southeastern Australia. *Geophysical Research Letters*, *42*, 7490–7497. https://doi.org/10.1002/2015GL065345

Kodaira, S., Nakamura, Y., Yamamoto, Y., Obana, K., Fujie, G., No, T., et al. (2017). Depth-varying structural characters in the rupture zone of the 2011 Tohoku-Oki earthquake. *Geosphere*, *13*(5), 1408–1424.

Koketsu, K., Miyake, H., & Suzuki, H. (2012, September). Japan integrated velocity structure model version 1. In *Proceedings of the 15th World Conference on Earthquake Engineering (No. 1773)*. Lisbon.

Kugler, S., Bohlen, T., Forbriger, T., Bussat, S., & Klein, G. (2007). Scholte-wave tomography for shallow-water marine sediments. *Geophysical Journal International*, *168*(2), 551–570.

Li, D., Helmberger, D., Clayton, R. W., & Sun, D. (2014). Global synthetic seismograms using a 2-D finite-difference method. *Geophysical Journal International*, *197*(2), 1166–1183.

Lindsey, N. J., Dawe, T. C., & Ajo-Franklin, J. B. (2019). Illuminating seafloor faults and ocean dynamics with dark fiber distributed acoustic sensing. *Science*, *366*(6469), 1103–1107.

Longuet-Higgins, M. S. (1950). A theory of the origin of microseisms. *Philosophical Transactions of the Royal Society of London A: Mathematical, Physical and Engineering Sciences*, *243*(857), 1–35.

Martin, E. R., Lindsey, N., Ajo-Franklin, J., & Biondi, B. (2018). Introduction to interferometry of fiber optic strain measurements. EarthArXiv.

Minoura, K., Sugawara, D., Yamanoi, T., & Yamada, T. (2015). Aftereffects of subduction-zone earthquakes: Potential tsunami hazards along the Japan sea coast. *The Tohoku Journal of Experimental Medicine*, *237*(2), 91–102.

Miyazawa, M., Snieder, R., & Venkataraman, A. (2008). Application of seismic interferometry to extract *P*- and *S*-wave propagation and observation of shear-wave splitting from noise data at Cold Lake, Alberta, Canada. *Geophysics*, *73*(4), D35–D40.

Mordret, A., Landès, M., Shapiro, N., Singh, S., & Roux, P. (2014). Ambient noise surface wave tomography to determine the shallow shear velocity structure at valhall: Depth inversion with a neighbourhood algorithm. *Geophysical Journal International*, *198*(3), 1514–1525.

Mordret, A., Landès, M., Shapiro, N. M., Singh, S. C., Roux, P., & Barkved, O. I. (2013). Near-surface study at the Valhall oil field from ambient noise surface wave tomography. *Geophysical Journal International*, *193*, 1627–1643.

Munn, J. D., Coleman, T. I., Parker, B. L., Mondanos, M. J., & Chalari, A. (2017). Novel cable coupling technique for improved shallow distributed acoustic sensor VSPs. *Journal of Applied Geophysics*, *138*, 72–79.

Muyzert, E. (2000). Scholte wave velocity inversion for a near surface *S*-velocity model and *PS*-statics. In *SEG Technical Program Expanded Abstracts 2000* (pp. 1197–1200). Society of Exploration Geophysicists. https://doi.org/10.1190/1.1815606

Nakamura, T., & Hayashimoto, N. (2018). Rotation motions of cabled ocean-bottom seismic stations during the 2011 Tohoku Earthquake and their effects on magnitude estimation for early warnings. *Geophysical Journal International*, *216*(2), 1413–1427.

Nakamura, Y., Kodaira, S., Cook, B. J., Jeppson, T., Kasaya, T., Yamamoto, Y., et al. (2014). Seismic imaging and velocity structure around the JFAST drill site in the Japan Trench: low V_P, high V_P/V_S in the transparent frontal prism. *Earth, Planets and Space*, *66*(1), 121.

Nolet, G., & Dorman, L. M. (1996). Waveform analysis of Scholte modes in ocean sediment layers. *Geophysical Journal International*, *125*(2), 385–396.

Oren, C., & Nowack, R. L. (2016). Seismic body-wave interferometry using noise auto-correlations for crustal structure. *Geophysical Journal International*, *208*, 321–332.

Perton, M., Spica, Z., & Caudron, C. (2017). Inversion of the horizontal-to-vertical spectral ratio in presence of strong lateral heterogeneity. *Geophysical Journal International*, *212*(2), 930–941.

Pham, T., & Tkalčić, H. (2017). On the feasibility and use of teleseismic *P* wave coda autocorrelation for mapping shallow seismic discontinuities. *Journal of Geophysical Research: Solid Earth*, *122*, 3776–3791. https://doi.org/10.1002/2017JB013975

Posey Jr., R., Johnson, G. A., & Vohra, S. T. (2000). Strain sensing based on coherent Rayleigh scattering in an optical fibre. *Electronics Letters*, *36*(20), 1.

Ritzwoller, M. H., & Levshin, A. L. (2002). Estimating shallow shear velocities with marine multicomponent seismic data. *Geophysics*, *67*(6), 1991–2004. https://doi.org/10.1190/1.1527099

Romero, P., & Schimmel, M. (2018). Mapping the basement of the Ebro Basin in Spain with seismic ambient noise autocorrelations. *Journal of Geophysical Research: Solid Earth*, *123*, 5052–5067. https://doi.org/10.1029/2018JB015498

Ruigrok, E., & Wapenaar, K. (2012). Global-phase seismic interferometry unveils *P*-wave reflectivity below the Himalayas and Tibet. *Geophysical Research Letters*, *39*, L11303. https://doi.org/10.1029/2012GL051672

Sanchez-Sesma, F. J. (1987). Site effects on strong ground motion. *Soil Dynamics and Earthquake Engineering*, *6*(2), 124–132.

Saygin, E., Cummins, P. R., & Lumley, D. (2017). Retrieval of the *P* wave reflectivity response from autocorrelation of seismic noise: Jakarta Basin, Indonesia. *Geophysical Research Letters*, *44*, 792–799. https://doi.org/10.1002/2016GL071363

Schalkwijk, K., Wapenaar, C., & Verschuur, D. (2000). Decomposition of multicomponent ocean-bottom data: Inversion for the sub-bottom parameters. In *SEG Technical Program Expanded Abstracts 2000*, (pp. 1205–1208). Society of Exploration Geophysicists. https://doi.org/10.1190/1.1815608

Schimmel, M., & Paulssen, H. (1997). Noise reduction and detection of weak, coherent signals through phase-weighted stacks. *Geophysical Journal International*, *130*(2), 497–505.

Scholte, J. G. J. (1958). *Rayleigh waves in isotropic and anistropic elastic media. Mededelingen en verhandelingen, KNMI*, *72*, 9–43.

Shinohara, M., Fukano, T., Kanazawa, T., Araki, E., Suyehiro, K., Mochizuki, M., et al. (2008). Upper mantle and crustal seismic structure beneath the northwestern Pacific Basin using a seafloor borehole broadband seismometer and ocean bottom seismometers. *Physics of the Earth and Planetary Interiors*, *170*(1-2), 95–106.

Shinohara, M., Machida, Y., Yamada, T., Nakahigashi, K., Shinbo, T., Mochizuki, K., et al. (2012). Precise aftershock distribution of the 2011 off the Pacific coast of Tohoku Earthquake revealed by an ocean-bottom seismometer network. *Earth, Planets and Space*, *64*(12), 8.

Shinohara, M., Yamada, T., Akuhara, T., Mochizuki, K., Sakai, S., Hamakawa, M., et al. (2019). Distributed Acoustic Sensing measurement by using seafloor optical fiber cable system off Sanriku for seismic observation. In *OCEANS 2019 MTS/IEEE SEATTLE* (pp. 1–4). Seattle, WA: IEEE. https://doi.org/10.23919/OCEANS40490.2019.8962757

Shinohara, M., Yamada, T., Sakai, S., Shiobara, H., & Kanazawa, T. (2016). Development and installation of new seafloor cabled seismic and tsunami observation system using ICT. In *OCEANS 2016 MTS/IEEE Monterey* (pp. 1–4). Monterey, CA: IEEE. https://doi.org/10.1109/OCEANS.2016.7761350

Sladen, A., Rivet, D., Ampuero, J.-P., De Barros, L., Hello, Y., Calbris, G., & Lamare, P. (2019). Distributed sensing of earthquakes and ocean-solid earth interactions on seafloor telecom cables. *Nature Communications*, *10*(1), 1–8.

Socco, V. L., Boiero, D., Maraschini, M., Vanneste, M., Madshus, C., Westerdahl, H., et al. (2011). On the use of the Norwegian Geotechnical Institute's prototype seabed-coupled shear wave vibrator for shallow soil characterization-II. Joint inversion of multimodal Love and Scholte surface waves. *Geophysical Journal International*, *185*(1), 237–252.

Spica, Z. J., Legrand, D., Iglesias, A., Walter, T. R., Sebastian, H., Dahm, T., et al. (2015). Hydrothermal and magmatic reservoirs at Lazufre volcanic area, revealed by a high-resolution seismic noise tomography. *Earth and Planetary Science Letters*, *421*, 27–38. https://doi.org/10.1016/j.epsl.2015.03.042

Spica, Z. J., Perton, M., Nakata, N., Liu, X., & Beroza, G. C. (2017). Site characterization at Groningen gas field area through joint surface-borehole H/V analysis. *Geophysical Journal International*, *212*(1), 412–421. https://doi.org/10.1093/gji/ggx426

Sun, W., & Kennett, B. (2016). Receiver structure from teleseisms: Autocorrelation and cross correlation. *Geophysical Research Letters*, *43*, 6234–6242. https://doi.org/10.1093/gji/ggx426

Suzuki, W., Aoi, S., Sekiguchi, H., & Kunugi, T. (2011). Rupture process of the 2011 Tohoku-Oki mega-thrust earthquake (M9.0) inverted from strong-motion data. *Geophysical Research Letters*, *38*, L00G16. https://doi.org/10.1029/2011GL049136

Taylor, G., Rost, S., & Houseman, G. (2016). Crustal imaging across the North Anatolian Fault Zone from the autocorrelation of ambient seismic noise. *Geophysical Research Letters*, *43*, 2502–2509. https://doi.org/10.1002/2016GL067715

Tonegawa, T., Fukao, Y., Nishida, K., Sugioka, H., & Ito, A. (2013). A temporal change of shear wave anisotropy within the marine sedimentary layer associated with the 2011 Tohoku-Oki earthquake. *Journal of Geophysical Research: Solid Earth*, *118*, 607–615. https://doi.org/10.1002/jgrb.50074

Vardy, M. E., Vanneste, M., Henstock, T. J., Clare, M. A., Forsberg, C. F., & Provenzano, G. (2017). State-of-the-art remote characterization of shallow marine sediments: the road to a fully integrated solution. *Near Surface Geophysics*, *15*(4), 387–402.

Williams, E. F., Fernández-Ruiz, M. R., Magalhaes, R., Vanthillo, R., Zhan, Z., González-Herráez, M., & Martins, H. F. (2019). Distributed sensing of microseisms and teleseisms with submarine dark fibers. *Nature Communications*, *10*(1), 1–11.

Yao, H., Gouedard, P., Collins, J. A., McGuire, J. J., & van der Hilst, R. D. (2011). Structure of young East Pacific Rise lithosphere from ambient noise correlation analysis of fundamental-and higher-mode Scholte-Rayleigh waves. *Comptes Rendus Geoscience*, *343*(8-9), 571–583.